IEEE Access
Multidisciplinary ⋮ Rapid Review ⋮ Open Access Journal

Received 14 April 2025, accepted 14 May 2025, date of publication 21 May 2025, date of current version 29 May 2025.

Digital Object Identifier 10.1109/ACCESS.2025.3572293

RESEARCH ARTICLE

Active Voltage Quadrupler Rectifier-Based Ultra-High Boost Ratio Multidirectional Energy Router in 800 V DC Microgrids

YUCHONG PENG, (Student Member, IEEE), JIAWEI LIANG, (Student Member, IEEE), AND HAOYU WANG, (Senior Member, IEEE)
School of Information Science and Technology, ShanghaiTech University, Shanghai 201210, China
Corresponding author: Haoyu Wang (wanghy@shanghaitech.edu.cn)

This work was supported in part by the National Natural Science Foundation of China under Grant 52077140, and in part by the Shanghai Rising Star Program under Grant 20QA1406700.

ABSTRACT In 800V DC microgrids, an energy router is essential for managing power distribution among the low-voltage photovoltaic (PV) panel, energy storage battery, and high-voltage dc link. Current solutions face challenges in simultaneously achieving high step-up ratios, multidirectional power flow, and maintaining high efficiency across broad input voltage and load ranges. To address these issues, this paper introduces a novel energy router featuring three key innovations. First, it combines an interleaved boost converter with an active voltage quadrupler cell (VQC), reducing voltage stress by 50% compared to conventional designs. Second, it employs an integrated magnetic design that utilizes leakage inductance, reducing magnetic volume by 36%. Third, it uses hybrid modulation, merging pulse-width modulation (PWM) and phase-shift modulation (PSM), to optimize switching and circulating losses while minimizing transformer turns and total power loss. Additionally, this configuration halves the voltage stress experienced by the MOSFETs on the high-voltage side relative to the dc link voltage. A 500W prototype was developed and tested, interfacing with a 15-25 V PV port, 40-50 V battery port, and 800 V dc link. Experimental results demonstrate a peak efficiency of 97.5% with stable operation under 0-100% load transitions. Comprehensive analysis, including dynamic studies (working modes switching, 95% load step changes) confirms the topology's reliability in 800V DC microgrid applications.

INDEX TERMS Energy router, high-voltage bus, multidirectional power flow, voltage multiplier, zero-voltage switching (ZVS).

I. INTRODUCTION

The global photovoltaic (PV) sector is pivotal to the ongoing energy transition, with installations exceeding 505 GW in 2024 and an anticipated global capacity approaching 10,000 GW by 2030 [1]. This rapid growth highlights the critical role of PV technology in the shift towards more sustainable energy sources. However, the intermittent nature of solar energy presents significant challenges, necessitating the integration of energy storage systems such as batteries to absorb surplus energy and ensure a stable power supply.

The associate editor coordinating the review of this manuscript and approving it for publication was Khaled Ahmed.

Traditionally, the connection between PV panels, energy storage units and loads has been facilitated through multiple discrete converters [2], [3]. While functional, this approach introduces several drawbacks, including reduced efficiency due to multilevel energy transmission, increased system complexity due to individual control of multiple converters, and decreased power density due to the proliferation of components. To mitigate these issues, integrated energy routers have emerged as a promising solution [4]. By consolidating multiple input and output ports into a single converter, the energy router simplified the power flow through fewer transmission stages, enhancing system efficiency. This integration not only improves power density but also simplifies

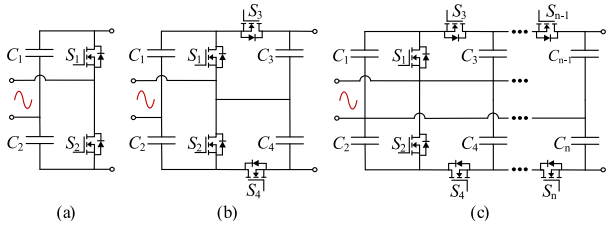

FIGURE 1. Symmetric active voltage multiplier cell in even derivation.(a) Voltage doubler cell. (b) Voltage quadrupler cell; (c) *n*-stage voltage multiplier cell.

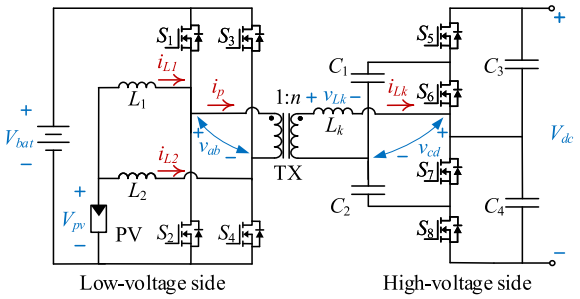

FIGURE 2. Schematic of the proposed energy router.

system design and control, reducing costs and increasing reliability [5].

According to the galvanic isolation scheme, energy routers can be classified into non-isolated, fully isolated, and partially isolated types. Non-isolated energy routers are compact and cost-effective but are not suitable for high-voltage (HV) or safety-critical applications due to the absence of galvanic isolation [6], [7]. Fully isolated energy routers, on the other hand, are typically larger and more costly because of the inclusion of bulkier magnetic components and additional switching devices [8], [9], [10]. In contrast, partially isolated energy routers provide a balanced solution. They offer galvanic isolation between the low-voltage (LV) and HV sides, rather than across all ports. This makes them particularly suitable for renewable energy applications, such as distributed PV systems, where isolation between the PV panel and the battery is not always required [11], [12], [13], [14], [15], [16], [17].

Typically, the structure of partially isolated energy routers consists of two common-grounded inverters on the LV side, an isolated transformer with a turn ratio of 1:*n*, and a secondary side rectifier. On the LV side, a boost circuit is added to each input port [11] to achieve high boost ratio. Additionally, [12] integrates a boost circuit with a full-bridge converter to reduce the component count by reusing the bridge arms. A hybrid structure, combining an interleaved boost stage with a full-bridge converter, is introduced in [13], [17], and [18]. This configuration minimizes input current ripple, reduces stress on the input components, and efficiently regulates the power exchange between the PV and battery ports.

For the secondary side, an active full-bridge rectifier rather than a classical full-bridge rectifier [19], is used to transfer power with mitigated conduction losses in [20]. In [21], a current-fed full-bridge converter connects the PV and load/grid ports, with diodes replacing the upper bridge arm's active MOSFETs to reduce circulating current and minimize voltage stress on the secondary side.

Voltage multiplier topologies, such as those used in [22], [23], and [24], leverage cascading structures to achieve high voltage levels, reduce output voltage drop and ripple, and extend the voltage step-up range, thereby enhancing their suitability for HV applications [25]. Among these, even-order active voltage multiplier derivations, as illustrated in Fig. 1, are commonly employed in high step-up converters due to their ability to provide symmetrically balanced voltage stress on both capacitors and switches. Fig. 1(a) shows a voltage doubler cell [14], [15], [16], Fig. 1(b) depicts a voltage quadrupler cell (VQC) [26], [27], [28], [29], [30], [31], [32], and Fig. 1(c) illustrates the derivation of an *n*-stage voltage multiplier cell [33], [34]. Among them, the voltage quadrupler cell offers an optimal balance between voltage step-up ratio and component count, making it a preferred solution in HV energy routers. To improve, we propose a novel active voltage quadrupler rectifier based on a partially isolated energy router in [35]. This article is the extension of the conference version.

Recent advancements in microgrid technology emphasize the integration of electric vehicles (EVs) as both dynamic loads and energy storage units. Through vehicle-to-grid (V2G) technology, EVs serve as controllable energy assets, enhancing frequency stability and load flexibility in renewable-based microgrids. For example, an FO-fuzzy PSS strategy optimized by an adaptive sine cosine algorithm (a-SCA) mitigates frequency deviations in PV-integrated EV microgrids [36]. Additionally, energy management strategies (EMS) reducing; converter counts-such as those in hybrid PV-PEMFC systems are being adopted to improve compactness and simplify control complexity [37]. These trends highlight the growing need for integrated, scalable power converter solutions that adapt to diverse power flow conditions while maintaining efficiency and controllability, aliening with the motivation and design of the proposed energy routers in this work.

The schematic of the proposed energy router is plotted in Fig. 2. It benefits from the interleaved boost stage's reduced input current ripple and utilizes an active VQC to achieve bidirectional power flow with a high boost ratio. This combination reduces voltage stress on the switching devices, contributing to improved system reliability and efficiency. A pulse-width modulation (PWM) scheme combined with phase-shift modulation (PSM) is introduced to balance the zero voltage switching (ZVS) range and minimize the root mean square (RMS) current across all operating modes, further enhancing efficiency. Additionally, integrating the inductor and transformer into a unified structure reduces the converter's physical size, providing a compact and cost-effective solution. The major extra contributions include:

1) A detailed analysis of circulating current and soft-switching conditions is provided, improving efficiency by suppressing RMS current and operating in the ZVS region.
2) A comprehensive analysis of the operating principles and design guidelines is presented. The compact size is achieved by using the transformer's leakage inductance as the series inductor, significantly reducing the size of magnetic components and the converter, thus enhancing power density. Control strategies are also summarized, and the control block diagram is provided.
3) Extensive experimental results across different modes are presented to validate the proposed concept. The dynamic response, ZVS performance, and efficiency at various input voltages are discussed. A thorough comparison with other partially isolated energy routers and high-boost ratio converters is provided to highlight the advantages of the proposed design.

The manuscript is structured as follows: Section II describes the proposed topology and its operation modes. Section III presents a detailed analysis of six fundamental operation modes, including their operational principles. Section IV analyzes the normalized power and ZVS range. The experimental results validating the theoretical analysis and the performer comparison are reported in Section V. Finally, Section VI concludes this work.

II. OPERATION PRINCIPLES

A. TOPOLOGY DERIVATION

Fig. 2 illustrates the schematic of the proposed energy router. The battery and dc bus both supply and absorb power, while the PV source only provides power.

On the LV side, a hybrid stage is employed, combining a full-bridge converter and an interleaved boost stage. LV side is equipped with two inductors (L_1 and L_2) and four power MOSFETs (S_1 to S_4). The gate signals for S_1 and S_2 (S_3 and S_4) are complementary, with dead times introduced to ensure proper switching. The two parallel phase legs are driven with a 180° phase shift to achieve interleaving. The duty cycle of the gate signal for S_1 is denoted as D, and it regulates the boost ratio between the PV panel and the battery.

The transformer turns ratio is defined as $1{:}n$. L_k is the series inductance which is implemented by the transformer leakage inductance. The primary current i_p is n times the secondary current i_{L_k}.

On the HV side, an active quadrupler cell is employed, derived from passive voltage multipliers. The rectifier is responsible for power conversion in the forward direction, from the input to the dc bus, while the inverter manages the reverse path. The active voltage multiplier cell enables phase-shifting control and bidirectional power flow between the LV and HV sides. The gate signals for MOSFETs S_5 and S_6 (S_7 and S_8) are complementary, with appropriate dead times. The duty cycle for S_5 and S_7 is fixed at 0.5. Moreover, a phase shift of φ is applied between the switching patterns of S_4 and S_5 to regulate the power delivered to the dc bus.

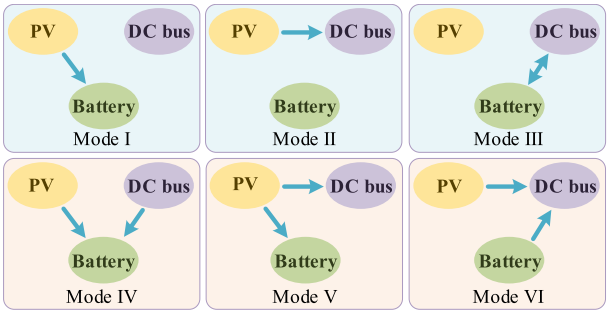

FIGURE 3. Main operating modes.

B. OPERATION MODES

For a energy router-based grid-tied PV-battery system, six main operation modes (see Fig. 3) are necessary for a typical day, all of which can be achieved by the proposed energy router. These modes are designed to optimize power management between the PV panel, the battery, and the dc grid, ensuring that the system operates efficiently under varying conditions [4]. Defining the output power of PV panels, release or absorb the power of batteries, and dc bus demand power as P_{pv}, P_{bat} and P_{dc} respectively. The basic power balance of an energy router architecture can be expressed as follows

$$P_{dc} = P_{pv} + P_{bat}. \tag{1}$$

The operation modes can be classified into two categories based on the number of active ports. In Modes I-III, the converter functions as a two-port converter, while in Modes IV-VI, it operates as a multidirectional energy router.

Mode I: dc bus is offline, and the PV panel generates power that is delivered unidirectionally to the battery.

Mode II: Battery is inactive, and the PV panel generates power that is delivered through the transformer to the dc bus.

Mode III: PV panel is idle during the night and the power flows bidirectionally between the battery and the dc bus, which is defined as forward and backward mode. This enables the battery to provide power to the dc grid to compensate for peak demand, while excess energy from the dc grid can be stored in the battery.

Modes IV–VI: All three ports are active. The PV panel generates power, which can be delivered unidirectionally to either the battery or the dc bus. Power flow between the two sides of the transformer is bidirectional, regulated by the load demand of the dc grid and the state of charge of the battery. Thus, the system operates in six distinct modes based on the power relationships among the three ports. It is important to note that even in two-port mode, where there is no net power flow from the battery port or PV port, it remains operational and affects the energy router's behavior.

III. MODE ANALYSIS

A. MODE I

In Mode I, the energy router operates on the LV side with the dc bus inactive, directing all power from the photovoltaic

source to charge the battery. In this mode, the HV side MOSFETs remain off, and the energy router behaves like an interleaved boost converter. The driving signals for S_1 and S_2 (S_3 and S_4) are complementary, with a dead time (t_d) introduced, and are driven in an interleaved manner with regulated duty cycles and a 180° phase shift. The duty cycle of the higher side MOSFETs (S_1, S_3) is denoted as D. On the LV side, a three-level voltage v_{ab} with duty cycle D is generated due to PWM control. The duty cycle D is adjusted to perform Maximum Power Point Tracking (MPPT) based on the battery voltage and PV operating conditions.

The interleaved boost converter establishes a direct relationship between the PV source voltage (V_{pv}) and the battery voltage (V_{bat})

$$V_{bat} = \frac{V_{pv}}{D}. \tag{2}$$

The minimum valley values of the inductor currents, i_{L_1} and i_{L_2}, are given by

$$i_{L_1.\min} = i_{L_2.\min} = \frac{1}{2}\left(\frac{P_{pv}}{V_{pv}} - \frac{V_{pv}(1-D)}{L_1 f_s}\right) \tag{3}$$

where f_s is the switching frequency.

B. MODES II AND III

These two modes are analyzed together as their power flow occurs between the LV side and the HV side. The voltage at the LV side, either from the PV or the battery, through the full-bridge or interleaved boost stage, is represented by v_{ab}.

In Mode II, the battery is offline, and the PV panel generates power to the dc bus via the interleaved boost stage (using PWM) and an active VQC.

In Mode III, during nighttime operation when the PV source is inactive, power flows bidirectionally between the battery and the dc bus to manage the battery state of charge and provide grid power. This mode combines a full bridge and an active VQC.

Power flow in both modes is mainly controlled by phase-shift modulation, with the converter operating in either forward or backward mode. Furthermore, the primary and secondary sides of the converter are connected through a transformer with a turns ratio of 1:n. Notably, even when the PV port is inactive in Mode III, the interleaved boost still operates with interleaved currents, although the current bias is zero. Following the principles governing the HV side MOSFETs, the relationship between the amplitude of V_{cd} and V_{dc} is given by

$$V_{cd} = \frac{V_{dc}}{4}. \tag{4}$$

The relationship between the amplitude of V_{pv} and V_{dc} is expressed as

$$V_{dc} = \frac{4nV_{pv}}{D}. \tag{5}$$

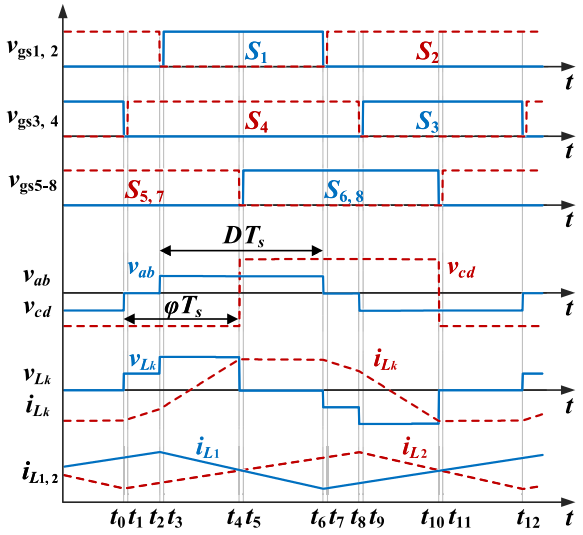

FIGURE 4. Critical steady-state waveforms.

C. MODES IV-VI

Steady-state operation of the proposed energy router combines LV side PWM with HV side phase-shift modulation, which depends on the values of $D < 0.5$ and φ. Based on the range of D and φ, the system exhibits 8 distinct steady-state operations. This analysis focuses on the operational state characterized by $D < 0.5$ and $0.5-D \leq \varphi < 0.5$. Within this state, the system operates in 12 distinct states over one switching period. Key waveforms are shown in Fig. 4, and the corresponding equivalent circuits are provided in Fig. 5. Inductors L_1 and L_2 are designed with equal values to support continuous inductor currents.

Combining equations (2) and (4), the voltage conversion ratio M is defined as

$$M = \frac{V_{dc}}{4nV_{bat}}. \tag{6}$$

The conversion ratio M adapts to variations in V_{pv} through different D values, ensuring voltage matching, with the conversion ratio equal to 1.

State I [t_0, t_1): Before t_0, $S_{2,3}$ on the LV side and $S_{5,7}$ on the HV side are ON, and L_1 and L_2 are energized by the PV panel. i_{L_k} is negative and decreases. At t_0, S_3 is turned OFF, and v_{cd} is clamped at $V_{dc}/4$. In this state, i_{L_k} is given by

$$i_{L_k} = \frac{V_{dc}/4}{L_k}(t - t_0) + i_{L_k}(t_0). \tag{7}$$

State II [t_1, t_2): At t_1, S_4 is turned ON. C_2 and C_3 are charged, while C_1 is discharged. i_{L_k} continues to decrease at the same rate as in state I.

State III [t_2, t_3): At t_2, S_2 is turned OFF, and v_{ab} is clamped at V_{pv}/D. At t_3, i_{L_k} is expressed as

$$i_{L_k} = \frac{nV_{bat} + V_{dc}/4}{L_k}(t - t_2) + i_{L_k}(t_2). \tag{8}$$

State IV [t_3, t_4): At t_3, S_1 is turned ON, and i_{L_k} continues to increase at the same rate as in state III.

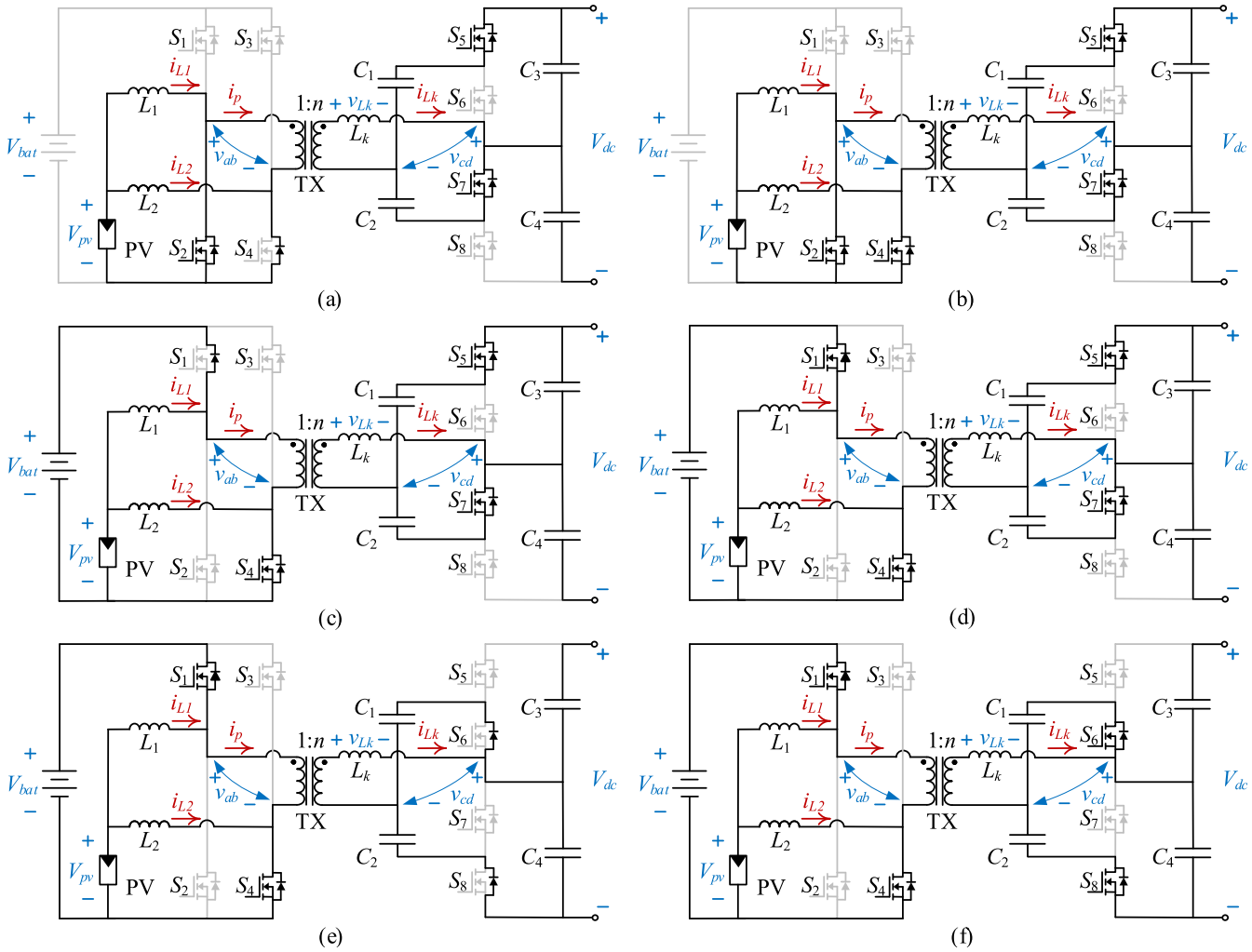

FIGURE 5. Equivalent circuits: (a) State I, $t_0 \le t < t_1$. (b) State II, $t_1 \le t < t_2$. (c) State III, $t_2 \le t < t_3$. (d) State IV, $t_3 \le t < t_4$. (e) State V, $t_4 \le t < t_5$. (f) State VI, $t_5 \le t < t_6$.

State V $[t_4, t_5)$: At t_4, S_5 and S_7 are turned OFF. i_{L_k} flows from the source to the drain of S_6 and S_8. In this state, i_{L_k} increases linearly as

$$i_{L_k} = \frac{nV_{bat} - V_{dc}/4}{L_k}(t - t_4) + i_{L_k}(t_4). \tag{9}$$

State VI $[t_5, t_6)$: The positive current of i_{L_k} contributes to the ZVS turn-on of S_6 and S_8. C_1 and C_4 are charged, while C_2 is discharged. i_{L_k} continues to decrease at the same rate as in state V.

Since states VII to XII are symmetric to states I to VI, we obtain the following relationship

$$i_{L_k}(t_0) = -i_{L_k}(t_6). \tag{10}$$

Combining equations (7)-(9), the inductor current expressions at different instants are derived as

$$\begin{aligned} i_{L_k}(t_0) &= -i_{L_k}(t_6) = I_N(M - 2D - 4M\varphi) \\ i_{L_k}(t_2) &= -i_{L_k}(t_8) = I_N(3M - 2D - 4M\varphi - 4DM) \\ i_{L_k}(t_4) &= -i_{L_k}(t_{10}) = I_N(M + 2D + 4\varphi - 2) \end{aligned} \tag{11}$$

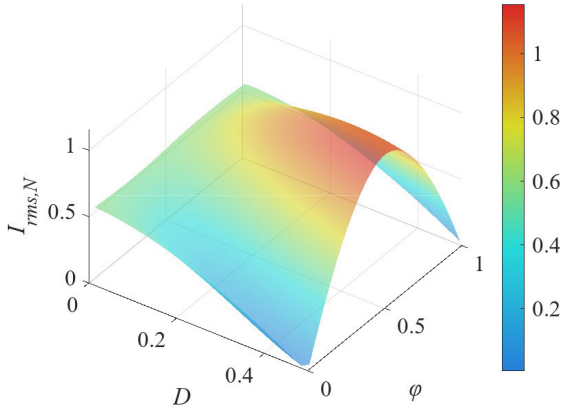

FIGURE 6. $I_{rms,N}$ varies from D and φ.

where I_N is the normalized current, defined as

$$I_N = \frac{nV_{bat}}{4f_sL_k}. \tag{12}$$

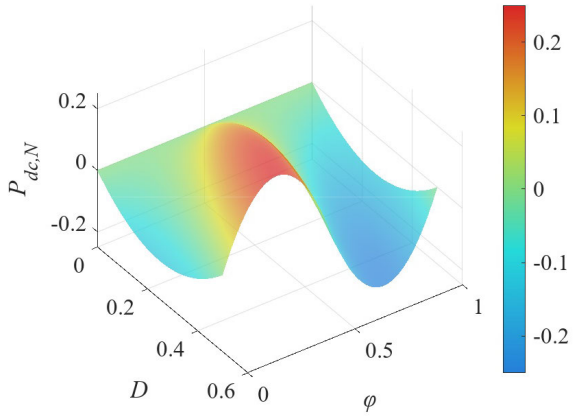

FIGURE 7. $P_{dc,N}$ versus D and φ.

Due to the symmetry of D with respect to 0.5 and φ with respect to 0, situations with different values of $0.5 < D < 1$ and $\varphi < 0$ can also be analyzed using the same method. These solutions serve as valuable tools for the power flow analysis and ZVS condition in Section IV.

The inductor current changes linearly within each steady-state period, and the current $i_{L_k}(t)$ can be derived accordingly. The normalized RMS current, $I_{rms,N}$, can be calculated by

$$I_{rms,N} = \frac{1}{I_N}\sqrt{f_s \int_{t_0}^{t_{12}} i_{L_k}^2(t)} \tag{13}$$

and is plotted in Fig. 6.

As φ increases, $I_{rms,N}$ initially increases, then decreases, and gradually transitions into a sinusoidal function. The variation of $I_{rms,N}$ with D exhibits three distinct trends when φ is between 0 and 0.5: first trend: $I_{rms,N}$ decreases and then increases as D increases; second, $I_{rms,N}$ continuously increases with D; and third, $I_{rms,N}$ continuously decreases with D. Specifically, when $D = 0.5$, $I_{rms,N}$ corresponds to the classic value of $I_{rms,N}$ for single-phase shift modulation. In the design process, conduction losses must be considered, so the values of D and φ should be chosen within the region where $I_{rms,N}$ remains relatively small to optimize efficiency.

IV. POWER FLOW AND ZVS ANALYSIS

A. OUTPUT POWER

In the analysis within the range $D < 0.5$ and $0.5-D \le \varphi < 0.5$, the dc bus power P_{dc} is calculated as

$$\begin{aligned} P_{dc}(D,\varphi) &= P_N P_{dc,N}(D,\varphi) \\ &= \frac{1}{T_s}\int_0^{T_s} v_{cd}(t)\cdot i_{L_k}(t)\,dt \\ &= P_N P_{dc,N}(0.5-D \le \varphi < 0.5) \\ &= P_N\left(2D^2 + 4D\varphi - 3D + 4\varphi^2 - 4\varphi + 1\right) \end{aligned} \tag{14}$$

where P_N is the normalized power, defined as

$$P_N = \frac{nV_{bat}V_{dc}}{8f_sL_k}. \tag{15}$$

Based on the values of D and φ, the normalized output power $P_{dc,N}$ is derived as

$$P_{dc,N}(D,\varphi) = \begin{cases} \sigma, & 0 \le \varphi < 0.5-D \\ -\sigma + 2D - (2\varphi-1)^2, & 0.5-D \le \varphi < 0.5 \\ -\sigma + 2D, & 0.5 \le \varphi < 1-D \\ \sigma - 4D + 4(\varphi-1)^2, & 1-D \le \varphi < 1 \end{cases} \tag{16}$$

where

$$\sigma = 2D^2 + 4D\varphi - D. \tag{17}$$

The output power function $P_{dc,N}$, based on the variation of D and φ, is plotted in Fig. 7. It is important to note that P_{dc} represents the dc bus demand power. Both P_{dc} and $P_{dc,N}$ share the same signs. When $P_{dc,N}$ is positive, the energy router operates in forward mode, and when $P_{dc,N}$ is negative, it operates in backward mode. The backward mode occurs in Modes III and IV.

By examining the relationship among $P_{dc,N}$, D, and φ, it can be observed that $P_{dc,N}$ first increases, then decreases, and increases again as φ increases. The maximum value of $P_{dc,N}$ gradually shifts from $\varphi = 0.5$ to $\varphi = 0.25$. The variation of $P_{dc,N}$ with D exhibits two distinct parabolic curves. From the formula of $P_{dc,N}$, it is evident that near the center, the curve is convex, while near the edges, it is concave. When $\varphi = 0$ or 1, $P_{dc,N}$ follows a parabolic shape concerning D and less than 0, indicating power transmission still occurs but in backward mode.

This formula can be used to adjust parameters for controlling both the magnitude and direction of power. The control strategy for the digital control block diagram in three-port modes is shown in Fig. 8.

B. CONTROL STRATEGIES AND IMPLEMENTATION

1) CONTROL STRATEGIES

The control diagram, shown in Fig. 8, generates PWM control signals for all MOSFETs based on the input voltage V_{pv} and current I_{pv}. The MPPT algorithm is first applied to determine the optimal power point. The duty cycle D for the LV side MOSFETs is calculated using equation (2), while the power values P_{pv} and P_{bat} are determined. The duty cycle D, along with the calculated dc power P_{dc} (derived from V_{dc} and I_{dc}), is substituted into equation (14) to compute φ. Finally, the PWM signals for both high- and LV sides are generated by comparing the values of φ and D, with the HV MOSFETs maintaining a fixed duty cycle of 0.5. The operation mode and modulation strategy are then determined by the operation mode unit.

The control diagram for different operating modes is shown in Fig. 9. The control process begins by evaluating

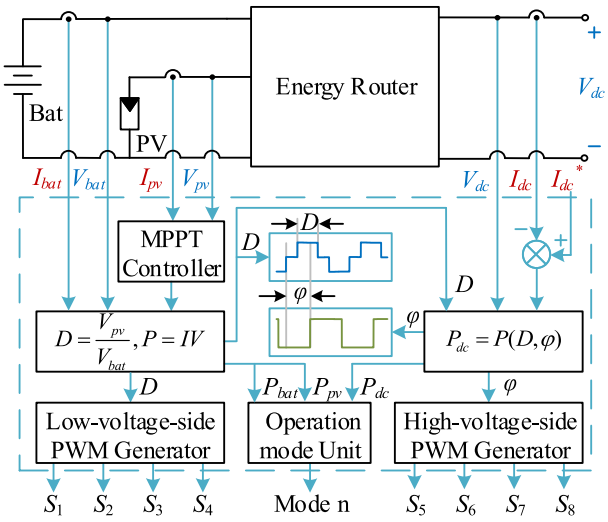

FIGURE 8. Block diagram of the digital controller. The diagram illustrates the logic flow of modulation parameter computation. Signal acquisition and PWM/PSM signal generation are implemented using the DSP (TMS320F28379D).

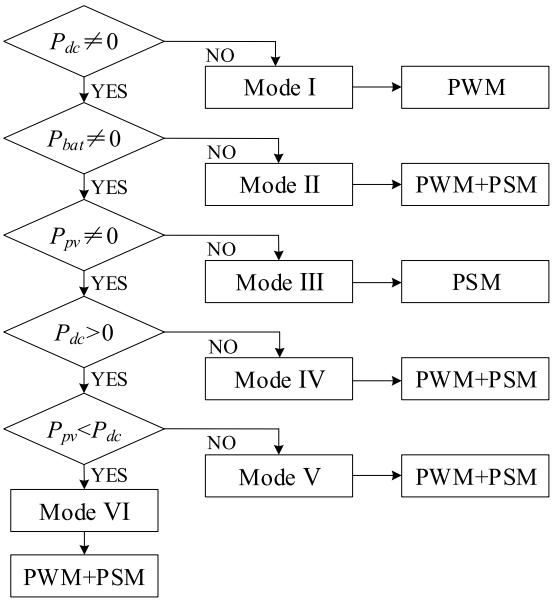

FIGURE 9. Operating mode flow chart.

the three power values: P_{pv}, P_{bat}, and P_{dc}. The energy router operates in at least two-port mode, meaning that at least two ports must have non-zero power values. The first step is to check whether P_{dc} is zero. If $P_{dc} = 0$, the system operates in Mode I, with power flow only between the LV ports, corresponding to interleaved parallel boost PWM modulation. If $P_{dc} \neq 0$, the next step is to check P_{bat}. If $P_{bat} = 0$, the system enters Mode II, requiring both PWM and PSM modulation. If $P_{bat} \neq 0$, the next check is P_{pv}. If $P_{pv} = 0$, Mode III is activated, where PWM is omitted, and only PSM modulation is used due to the unrestricted duty cycle D when $V_{pv} = 0$. If $P_{pv} \neq 0$, the direction of power flow is determined by the sign of P_{dc}: if $P_{dc} < 0$, Mode IV is activated; if $P_{dc} > 0$, the system enters either Mode V ($P_{pv} > P_{dc}$) or Mode VI ($P_{pv} < P_{dc}$). Modes IV–VI involve simultaneous operation of all three ports, requiring both PWM and PSM modulation.

2) IMPLEMENTATION DETAILS

The digital control system is implemented on a TI TMS320F28379D DSP, which is responsible for signal acquisition, control algorithm computation, and PWM/PSM signal generation. All voltage and current signals, including V_{pv}, I_{pv}, V_{bat}, I_{bat}, V_{dc}, and I_{dc}, are measured through Hall-effect sensors and sampled by the DSP's built-in 16-bit ADCs. The sampling and control loop operates at 100 kHz (10 μs control period), synchronized with the PWM carrier frequency,ensuring consistent timing and avoiding sampling-induced noise or delay errors.

The control algorithm flow, as shown in Fig. 8, is executed each cycle. The DSP first applies the MPPT algorithm based on V_{pv} and I_{pv}, then calculates the duty cycle D using (2). With the power values obtained (P_{pv}, P_{bat}, and P_{dc}), the phase-shift angle φ is computed using (14). The modulation parameters D and φ are used to generate synchronized PWM and PSM signals through the ePWM modules. High-voltage side MOSFETs operate with a fixed duty cycle of 0.5, while the timing of PSM signals is controlled with sub-microsecond precision using ePWM phase control. The system logic determines the operating mode and activates the corresponding modulation strategy via software flags and state machines.

To address implementation challenges, the resolution of the ePWM module (based on a 60 MHz clock) gives a timing resolution of 16.7 ns, which ensures sufficient precision for small phase-shift control. Sensitivity to phase-shift accuracy, especially under light-load conditions, is considered during DSP calibration. Additionally, component tolerances, particularly variations in transformer leakage inductance and output filter parameters, are considered by introducing margin in ZVS boundary calculations and performing real-time tuning if necessary.

C. ZVS CONDITION

1) HV SIDE MOSFETs

To ensure ZVS, C_{oss} of MOSFET should be fully discharged before the channel conducts. From an energy storage perspective, the minimum current required to charge and discharge the C_{oss} of two complementary MOSFETs in VQC is defined as

$$I_{ZVS1} = \sqrt{\frac{C_{oss(S_5-S_8)} V_{cd}^2}{2L_k}}. \tag{18}$$

To achieve ZVS, assuming I_{ZVS1} remains constant during the dead time, the following condition should be satisfied

$$I_{ZVS1} = V_{cd} C_{oss(S_5-S_8)} / t_d. \tag{19}$$

The current values of MOSFETs at the switching time derived in (11) should be larger than I_{ZVS}. Because of duty

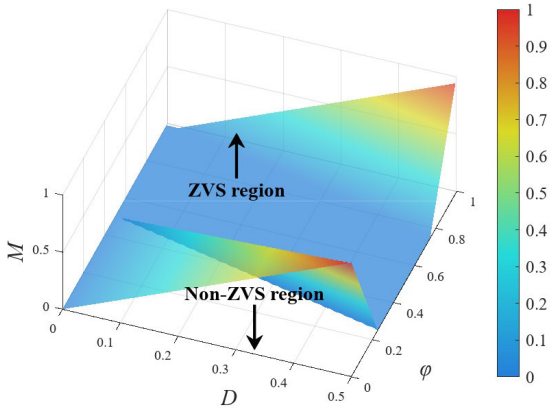

FIGURE 10. ZVS boundary of HV side MOSFETs S_5-S_8.

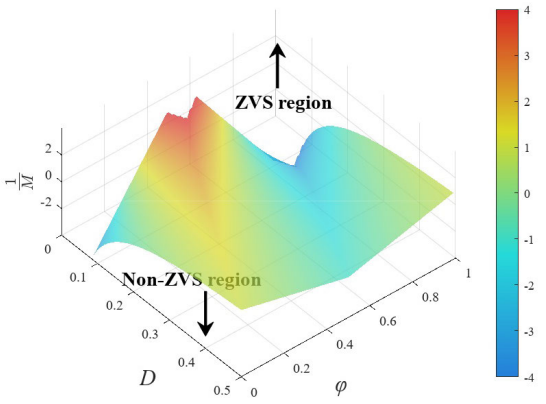

FIGURE 11. ZVS boundary of LV side MOSFETs S_1 and S_3.

cycle of HV side MOSFETs equals to 0.5 and symmetry properties, the ZVS condition of HV side MOSFETs can be calculated

$$i_{L_k}(t_4) = -i_{L_k}(t_{10}) > I_{ZVS1}. \tag{20}$$

Based on the range of D and φ, the ZVS boundary can be derived as

$$\begin{cases} I_N(M-2D) > I_{ZVS1}, & 0 \le \varphi < 0.5-D \\ I_N(M+2D+4\varphi-2) > I_{ZVS1}, & 0.5-D \le \varphi < 0.5 \\ I_N(-M-2D) > I_{ZVS1}, & 0.5 \le \varphi < 1-D \\ I_N(-M+2D+4\varphi-4) > I_{ZVS1}, & 1-D \le \varphi < 1. \end{cases} \tag{21}$$

The ZVS boundary of HV side MOSFETs is plotted in Fig. 10, and the curved surface depends on three parameters D, φ and M. Below the surface is non-ZVS region, and the above region is ZVS range. When M is less than 1, there is a non-ZVS region when φ is close to 0/1 and D is close to 0.5. It can be seen that ZVS is achieved over the entire range of the HV side MOSFETs when the conversion ratio M is greater than or equal to 1.

2) LV SIDE MOSFETs

According to the perspective of energy storage, the minimum current required to charge and discharge the C_{oss} of two complementary MOSFETs is defined as

$$I_{ZVS2} = \sqrt{2C_{oss}V_{bat}^2/L_k}. \tag{22}$$

To achieve ZVS, assuming I_{ZVS2} remains constant during the dead time, the following condition should be satisfied

$$I_{ZVS2} = 2V_{bat}C_{oss(S_1-S_4)}/t_d. \tag{23}$$

Because the primary current i_p, together with i_{L_1} and i_{L_2}, plays a crucial role in achieving soft switching for the primary-side switches, while the secondary-side switches are directly related to the secondary current i_{L_k}. The ZVS of LV side MOSFETs can be contributed by the interleaved boost

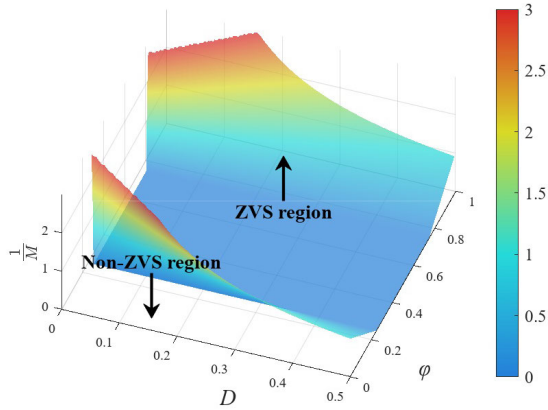

FIGURE 12. ZVS boundary of LV side MOSFETs S_2 and S_4.

units. As demonstrated in Fig. 5, the ZVS condition of the LV side MOSFETs can be expressed as

$$\begin{cases} S_1 : i_{L_1}(t_{S_1}) - ni_{L_k}(t_{S_1}) > I_{ZVS2} \\ S_2 : i_{L_1}(t_{S_2}) - ni_{L_k}(t_{S_2}) < -I_{ZVS2} \\ S_3 : i_{L_2}(t_{S_3}) + ni_{L_k}(t_{S_3}) > I_{ZVS2} \\ S_4 : i_{L_2}(t_{S_4}) + ni_{L_k}(t_{S_4}) < -I_{ZVS2} \end{cases} \tag{24}$$

where t_{S_1}-t_{S_4} correspond to the turn-ON instants of S_1-S_4, respectively. According to the basic principles of the boost converter, i_{L_1} and i_{L_2} are derived as

$$\begin{cases} i_{L_1}(t_{S_1}) = i_{L_2}(t_{S_3}) = \dfrac{P_{pv}}{2V_{pv}} + \dfrac{V_{pv}(1-D)}{2f_sL} \\ i_{L_1}(t_{S_2}) = i_{L_2}(t_{S_4}) = \dfrac{P_{pv}}{2V_{pv}} - \dfrac{V_{pv}(1-D)}{2f_sL}. \end{cases} \tag{25}$$

Based on basic interleaved boost converter principles and steady-state analysis of the LV side circuit, the ZVS range can

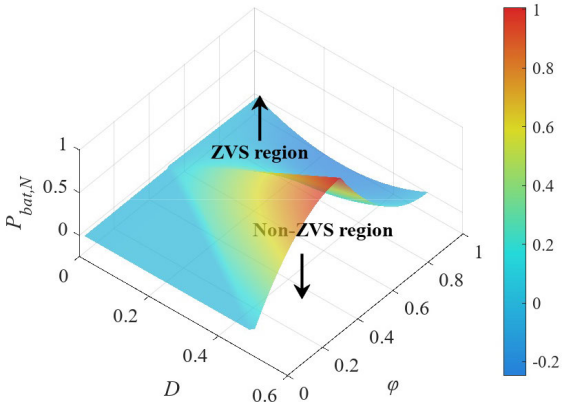

FIGURE 13. ZVS boundary of LV side MOSFETs vary with input power.

be derived as

$$\begin{cases} S_1 : P_{dc} + \gamma - 2(ni_{L_k}(t_2) + I_{ZVS2})DV_{bat} > P_{bat} \\ S_2 : P_{dc} - \gamma + 2(ni_{L_k}(t_0) + I_{ZVS2})DV_{bat} < P_{bat} \\ S_3 : P_{dc} + \gamma - 2(ni_{L_k}(t_2) + I_{ZVS2})DV_{bat} > P_{bat} \\ S_4 : P_{dc} - \gamma + 2(ni_{L_k}(t_0) + I_{ZVS2})DV_{bat} < P_{bat} \end{cases} \tag{26}$$

where γ defined as

$$\gamma = \frac{V_{bat}{}^2 D^2 (1-D)}{Lf_s}. \tag{27}$$

Combine (11), (14) and (26) the ZVS condition of low voltage side MOSFETs can be derived as equation (28), as shown at the bottom of the next page, an the parameters are D, φ, M and input power.

Therefore, the ZVS region varies with D, φ, M, and input power can be plotted in Fig. 11-13. The region above the surface represents the ZVS range, while the region below corresponds to the non-ZVS area. It is worth noting that the ZVS conditions for S_1 and S_3 are identical, as are those for S_2 and S_4. Fig. 13 illustrates the ZVS boundary of the low-voltage (LV) side MOSFETs as a function of the input power, derived from Eq. 28. Here, $P_{\text{bat},N}$ denotes the normalized battery power, defined as P_{bat}/P_N. The trend indicates that the normalized battery power $P_{bat,N}$ increase with φ from 0 to 0.5, and decrease with φ from 0.5 to 1.

D. LOSS ANALYSIS

Since all MOSFETs achieve ZVS during turn-ON, the main losses in the converter include MOSFET turn-OFF loss, conduction loss, and magnetic loss.

1) MOSFET TURN-OFF LOSS

Turn-OFF loss is significant due to the relatively high turn-OFF current under phase-shift control. Owing to the symmetry of the primary-side MOSFETs, the turn-OFF currents of S_1 and S_3 are equal, and similarly for S_2 and S_4. Therefore, only the turn-OFF currents of S_1 and S_2 are analyzed as follows:

$$\begin{aligned} i_{S1,\text{off}} &= -[i_{L1}(t_6) - ni_{Llk}(t_6)] \\ i_{S2,\text{off}} &= \quad [i_{L1}(t_2) - ni_{Llk}(t_2)] \end{aligned} \tag{29}$$

According to the basic principles of interleaved boost converters:

$$\begin{aligned} i_{L1}(t_2) &= \frac{P_{\text{pv}}}{2V_{\text{pv}}} + \frac{V_{\text{pv}}}{2L}(1-D)T_S \\ i_{L1}(t_6) &= \frac{P_{\text{pv}}}{2V_{\text{pv}}} - \frac{V_{\text{pv}}}{2L}(1-D)T_S \end{aligned} \tag{30}$$

By substituting equations (11) and (30) into (29), the turn-OFF currents can be expressed as:

$$\begin{aligned} i_{S1,\text{off}} &= \frac{DV_{\text{bat}}(1-D)}{2Lf_S} - \frac{P_{\text{pv}}}{2DV_{\text{bat}}} \\ &\quad + \frac{n^2 V_{\text{bat}}}{4L_{\text{lk}} f_S}(M - 2D - 4M\varphi) \\ i_{S2,\text{off}} &= \frac{DV_{\text{bat}}(1-D)}{2Lf_S} + \frac{P_{\text{pv}}}{2DV_{\text{bat}}} \\ &\quad + \frac{n^2 V_{\text{bat}}}{4L_{\text{lk}} f_S}(M + 2D + 4\varphi - 2) \end{aligned} \tag{31}$$

For the secondary-side MOSFET, due to the circuit symmetry and operating mode, the turn-off currents of S_5, S_6, S_7, and S_8 are equal in magnitude and opposite in direction:

$$i_{S5,\text{off}} = -i_{S6,\text{off}} = \frac{1}{2} i_{Llk}(t_4) = \frac{n^2 V_{\text{bat}}}{8L_{\text{lk}} f_S}(M + 2D + 4\varphi - 2) \tag{32}$$

During the turn-OFF transition, the turn-OFF loss occurs in two stages [33]. In the first stage (t_1), the drain-to-source voltage V_{ds} increases linearly from 0 to $V_{\text{ds,off}}$ while the current remains constant at i_{off}. In the second stage (t_2), the voltage remains constant at $V_{\text{ds,off}}$ while the current linearly decreases to zero. Although the energy stored in C_{oss} is recovered during the ZVS turn-ON process, it is subtracted from the turn-OFF energy loss.

Assuming linear waveforms, the turn-OFF power loss is calculated as:

$$P_{\text{loss,off}} = \left[\frac{V_{\text{ds,off}} \cdot i_{\text{off}}}{2}(t_1 + t_2) - \frac{1}{2} C_{\text{oss}} V_{\text{ds,off}}^2 \right] f_S \tag{33}$$

where t_1 and t_2 can be estimated from the MOSFET datasheet, f_S is the switching frequency, and $V_{\text{ds,off}}$ is the drain-to-source blocking voltage during turn-OFF. Therefore, reducing the turn-OFF current is essential to minimize the associated losses.

2) CONDUCTION LOSS OF SWITCHES

On the primary side, MOSFETs S_1 and S_3 (as well as S_2 and S_4) carry identical root-mean-square (RMS) currents due to circuit symmetry. On the secondary side, MOSFETs S_5–S_8 have identical RMS currents. The same applies to all

secondary-side diodes. Therefore, the total conduction loss can be expressed as:

$$P_{\text{cond}} = 2(R_1 I_{1,\text{rms}}^2 + R_1 I_{2,\text{rms}}^2 + 2R_2 I_{3,\text{rms}}^2) \tag{34}$$

where R_1 and R_2 are the ON-state resistances of the primary-side and secondary-side MOSFETs, respectively. $I_{1,\text{rms}}$, $I_{2,\text{rms}}$, and $I_{3,\text{rms}}$ are the RMS currents of S_1/S_3, S_2/S_4, and S_5–S_8, respectively.

3) CONDUCTION LOSS OF CAPACITORS

The conduction loss for each capacitor is calculated by:

$$P_{\text{loss,cap}} = R_{\text{ESR}} \cdot I_{\text{cap}}^2 \tag{35}$$

where R_{ESR} is the equivalent series resistance of the capacitor and I_{cap} is the RMS value of the ripple current.

4) GATE DRIVING LOSS

As described in [33], the gate driving loss for each MOSFET can be calculated by:

$$P_{\text{driv}} = V_{\text{DRV}} \cdot Q_G \cdot f_S \tag{36}$$

where V_{DRV} is the gate drive voltage and Q_G is the total gate charge.

5) MAGNETIC LOSS

The magnetic losses consist of copper (winding) losses and core losses. The copper loss is given by:

$$P_{\text{cu}} = \frac{\rho \cdot l_w}{A_w} \cdot I_{\text{rms}}^2 \tag{37}$$

where ρ, l_w, and A_w denote the resistivity, length, and cross-sectional area of the conductor, respectively. I_{rms} is the RMS current through the winding. It is worth noting that the use of Litz wire and interleaved winding helps reduce the skin and proximity effects.

The core loss is estimated using the Steinmetz equation:

$$P_{\text{fe}} = K_c f_S^{\alpha} (\Delta B/2)^{\beta} \tag{38}$$

where K_c, α, and β are Steinmetz parameters obtained from the magnetic core datasheet, and ΔB is the peak-to-peak magnetic flux density swing. ΔB can be calculated using Faraday's law of electromagnetic induction.

Additional losses, such as those caused by parasitic capacitance, leakage inductance, and PCB trace resistance, are collectively estimated to be approximately P_{other}.

Based on the above analysis, the total power losses are computed and illustrated in Fig. 14.

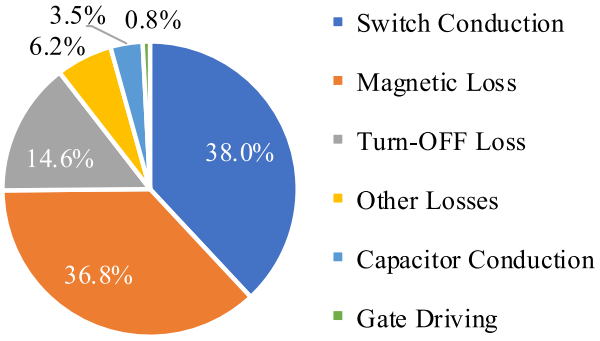

FIGURE 14. Power loss breakdown at rated power.

V. PARAMETER DESIGN METHODOLOGY

The proposed hybrid modulation scheme requires co-optimization of duty cycle D and phase shift φ to achieve three critical objectives:

1) Maintain zero-voltage switching (ZVS) across all active switches
2) Minimize circulating current (Fig. 6 and Fig. 15)
3) Ensure stable operation with at least 20% input voltage deviation

A. LEAKAGE INDUCTANCE OPTIMIZATION

Based on equations (12)–(20), the leakage inductance L_k plays a decisive role in determining converter performance:

$$\begin{cases} I_{\text{rms}} \propto \dfrac{1}{L_k} & \text{(Conduction loss)} \\ P_{\max} \propto \dfrac{1}{L_k} & \text{(Power transfer capacity)} \\ \text{ZVS}_{\text{range}} \propto \sqrt{L_k} & \text{(Soft-switching capability)} \end{cases} \tag{39}$$

A trade-off exists between conduction losses and soft-switching boundaries. A smaller L_k supports higher power and lower current, but at the cost of reduced ZVS range under light load. A final value of $L_k = 35\,\mu\text{H}$ is selected to balance these considerations, based on practical design optimization.

B. TRANSFORMER DESIGN

The integrated magnetic design incorporates both power transfer and leakage inductance functionalities within a single magnetic core, reducing total magnetic volume by 36%. Compared to a conventional design with 213.1 cm^3 volume [35], the proposed transformer occupies only 136.1 cm^3, as shown in Fig. 16 and summarized in Table 1.

The transformer turns ratio is derived from:

$$n = \frac{4V_{pv,\min}}{DV_{dc}} = \frac{4 \times 15}{D \times 800} = \left(\frac{0.3}{D}\right) : 4$$

$$\begin{cases} P_N\sigma - \gamma + 2(nI_N(M - 2D - 4M\varphi) + I_{ZVS2})DV_{bat} < P_{bat}, & 0 \le \varphi < 0.5 - D \\ P_N(-\sigma + 2D - (2\varphi - 1)^2) - \gamma + 2(nI_N(M - 2D - 4M\varphi) + I_{ZVS2})DV_{bat} < P_{bat}, & 0.5 - D \le \varphi < 0.5 \\ P_N(-\sigma + 2D) - \gamma + 2(nI_N(-3M - 2D + 4M\varphi) + I_{ZVS2})DV_{bat} < P_{bat}, & 0.5 \le \varphi < 1 - D \\ P_N(\sigma - 4D + 4(\varphi - 1)^2) - \gamma + 2(nI_N(-3M - 2D + 4M\varphi) + I_{ZVS2})DV_{bat} < P_{bat}, & 1 - D \le \varphi < 1. \end{cases} \tag{28}$$

TABLE 1. Magnetic component volume comparison.

Component	Conventional	Proposed
Transformer	136.1 cm^3	136.1 cm^3
Inductor	77 cm^3	Integrated
Total	213.1 cm^3	136.1 cm^3

TABLE 2. Comparison of component voltage stress in rectifier-based energy router.

Secondary-side Rectifier	MOSFETs & Diodes	Capacitors
Half-wave rectifier [14]	$2V_{dc}$	V_{dc}
Full-wave rectifier [18]	$2V_{dc}$	V_{dc}
Full-bridge rectifier [20]	V_{dc}	V_{dc}
This work	$V_{dc}/2$	$V_{dc}/2, V_{dc}/4$

For practical implementation, the turns ratio is set to 1:4. The core material is PC40, and the leakage inductance is adjusted by tuning the air gap between 0.5–1.2 mm. An interleaved winding structure is adopted to suppress AC resistance and improve high-frequency performance.

C. COMPONENT STRESS ANALYSIS

Table 2 compares voltage stresses across different rectifier topologies. The proposed VQC structure achieves a 50% reduction in MOSFET voltage stress (400 V vs. 800 V conventional). The improvement significantly enhances the reliability and efficiency of the system.

For practical implementation, 650 V/60 mΩ SiC MOSFETs (GC3M0060065K) were selected. Capacitor derating was applied with a high voltage rating (630 V caps for 420 V actual stress), ensuring long-term reliability and performance. These design choices strike a balance between component stress and system efficiency, making the proposed design suitable for high-performance applications.

D. A NUMERICAL DESIGN EXAMPLE

To demonstrate the parameter co-optimization process, a design case is presented for the condition $V_{\text{bat}} = 40-50$ V, $V_{\text{pv}} = 15-25$ V, with $D = 0.3 - 0.625$, targeting a nominal output power of 500 W.

Fig. 15(a) shows simulated power-φ curves under three different leakage inductance values: 15, 35, and 50 μH. Each curve intersects with the 500, 750, and 1000 W power line at some unique φ, which are then used to compute corresponding RMS currents. The results are plotted in Fig. 15(b).

Among all cases, $L_k = 35\,\mu$H results in the lowest RMS current of 2.90 A at 500 W. Therefore, 35 μH is selected as a balanced value ensuring full-range ZVS operation and moderate current stress.

The turns ratio n is obtained based on the lowest PV voltage and nominal DC bus voltage. With $D_{min} = 0.3$, the calculated ratio is:

$$n = \frac{4 \times 15}{0.3 \times 800} = \frac{60}{240} = 0.25 \Rightarrow 1:4$$

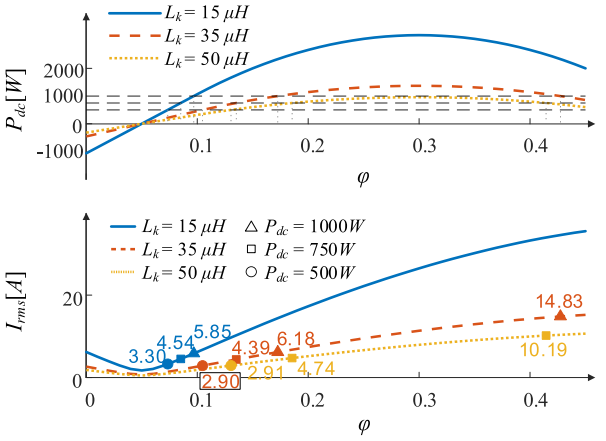

FIGURE 15. The relationship between the effective current I_{rms} [A] corresponding to different series inductance values $L_k = 15\mu H$, $35\mu H$, $50\mu H$ and different power values $P_{dc,N} = 1000W$, $750W$, $500W$ changes with φ.

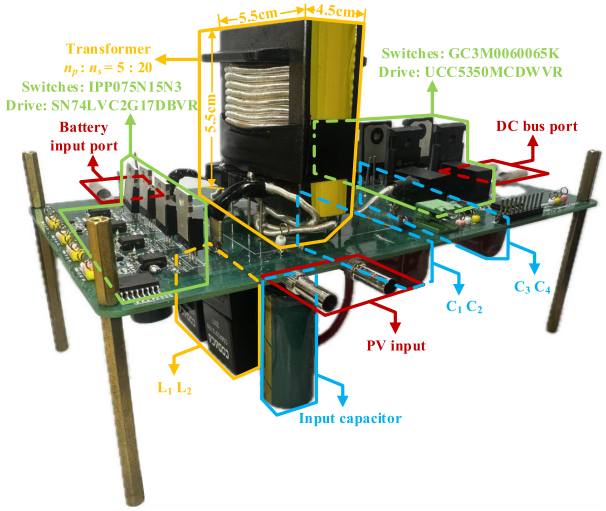

FIGURE 16. Photo of the designed prototype.

The transformer is implemented with a gapped PC40 core and interleaved windings, realizing a compact layout and low loss under hybrid modulation operation.

VI. EXPERIMENTAL RESULTS AND COMPARISON

To validate the effectiveness of the proposed energy router, a 500 W prototype is designed, with key design parameters listed in Table 3. The prototype is presented in Fig. 16. The PV source is emulated by a programmable dc power supply. The battery and dc bus are emulated by a programmable dc power source in parallel with an electric load. The digital control algorithm is implemented in TMS28379 microcontroller from Texas Instruments.

A. EXPERIMENTAL RESULTS

In Mode I, Fig. 17 shows the steady-state inductor current waveforms, highlighting a significant reduction in current ripple at the PV source due to the interleaved structure. PWM

TABLE 3. Design parameters.

Symbol	Description	Parameters
V_{pv}	PV voltage	15-40 V
V_{bat}	Battery voltage	40-50 V
V_{dc}	dc bus voltage	800 V
f_s	switching frequency	100 kHz
$L_{1,2}$	Buck/Boost inductor	80 μH
T	Transformer core	PC40
L_k	Leakage inductance of TX	35 μH
$n_p : n_s$	Winding ratio of TX	5:20
$C_1 - C_4$	HV side capacitor	3.3 μF
$S_1 - S_4$	LV side MOSFETs	IPP075N15N3
$S_5 - S_8$	HV side MOSFETs	GC3M0060065K

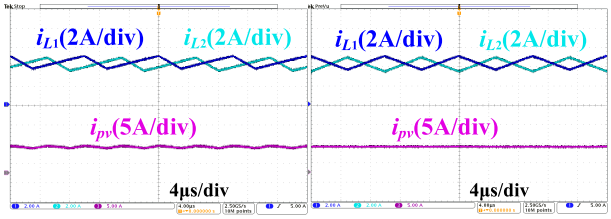

FIGURE 17. Mode I interleaved current waveforms (a) $V_{pv} = 15$ V, $V_{bat} = 50$ V, $P_{pv} = 150$ W. (b) $V_{pv} = 25$ V, $V_{bat} = 50$ V, $P_{pv} = 250$ W.

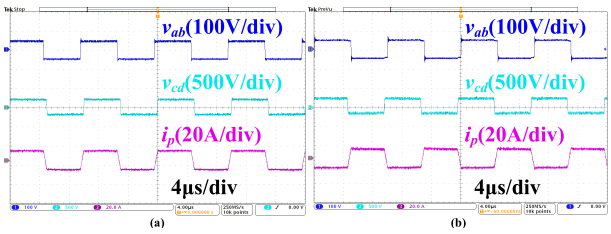

FIGURE 18. Steady-state waveforms in Mode III forward and backward power flow waveforms:(a) forward $V_{bat} = 50$ V, $V_{dc} = 800$ V, $P_{dc} = 500$ W; (b) backward $V_{bat} = 50$ V, $V_{dc} = 800$ V, $P_{dc} = -500$ W.

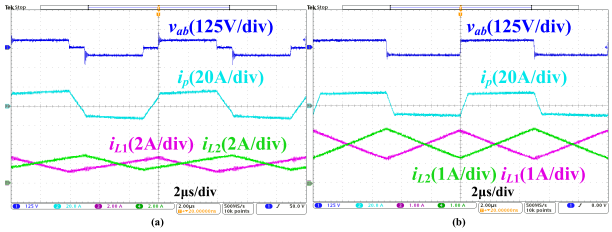

FIGURE 19. Steady-state waveforms in Mode VI when (a) $V_{pv} = 20$V, $V_{bat} = 50$V, $V_{dc} = 800$V, $P_{pv} = 160$W, $P_{dc} = 500$W. (b)$V_{pv} = 25$V, $V_{bat} = 50$V, $V_{dc} = 800$V, $P_{pv} = 200$W, $P_{dc} = 500$W.

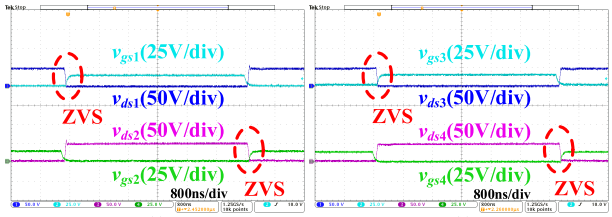

FIGURE 20. Soft-switching waveforms of the LV side MOSFETs of (a) $S_{1,2}$. (b) $S_{3,4}$.

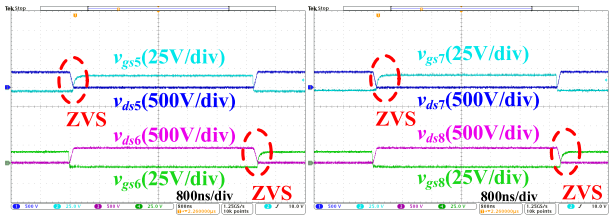

FIGURE 21. Soft-switching waveforms of the HV side MOSFETs of (a) $S_{5,6}$. (b) $S_{7,8}$.

control is employed in this mode, enabling MPPT of the PV source. Fig. 17(a) presents the waveforms with $V_{pv} = 15$ V, $V_{bat} = 50$ V, and $P_{pv} = 120$ W, resulting in a duty cycle D of 30%. In Fig. 17(b), with $V_{pv} = 25$ V, $V_{bat} = 50$ V, and $P_{pv} = 200$ W, the duty cycle of the LV side MOSFETs is 50%. Under these conditions, the current ripple from the PV source is effectively canceled.

The steady-state experimental waveforms for Mode III are shown in Fig. 18. The operating principles of Modes II-VI which using PWM plus PSM control are similar, with differences only in the power distribution among the three ports. Therefore, only the waveforms for Mode III and Mode VI are presented. In Mode III, the PV source is idle, and the average currents of i_{L_1} and i_{L_2} are zero. The power flow is controlled by the phase shift angle between the LV and HV sides. The side with the leading phase acts as the source, while the lagging side functions as the load. Fig. 18(a) presents the steady-state waveforms for forward power flow at 500 W. In contrast, Fig. 18(b) shows the steady-state waveforms for backward power flow at 500 W. The phase shift angles are determined using the equation 14, and the system operates within the ZVS region, as confirmed by the analysis results from equations (21) and (28).

Experimental waveforms of v_{ab}, i_p, i_{L_1}, and i_{L_2} for different PV voltages in three-port modes are shown in Fig. 19. Fig. 19(a) shows the experimental results in Mode VI, where the PV source provides 20 V and 160 W, while the dc bus absorbs 500 W. The excess power is supplied by the battery. The current ripple at the PV terminal is reduced due to the interleaved structure. Although ZVS is lost at this operating point, the RMS current remains relatively small, which results from a trade-off between switching losses and conduction losses. In Fig. 19(b), the PV source operates at 25 V and provides 200 W, with the battery supplying the remaining power. The waveforms illustrate that the sum of the currents through L_k, L_1, and L_2 contributes to achieving ZVS for the primary side MOSFETs. Additionally, the current through the series inductor aids in achieving ZVS for the active MOSFETs on the HV side.

Critical soft-switching waveforms for Modes IV–VI are shown in Figs. 20 and 21. As illustrated in Fig. 20, there is no overlap between the rising edge of v_{gs} and the falling edge of v_{ds}, confirming ZVS for the LV side MOSFETs (S_{1-4}). In Fig. 21, ZVS for the HV side MOSFETs (S_{5-8}) is also demonstrated. In this case, the v_{gs} of HV side MOSFETs experience a negative voltage during turn-off, and ZVS is still achieved as the devices turn on when the voltage across

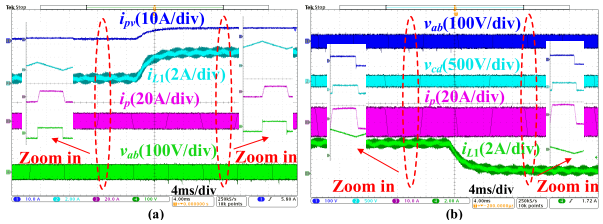

FIGURE 22. Dynamics when (a) PV power steps from 10 to 200 W in Mode VI. (b) mode transition Mode VI to III.

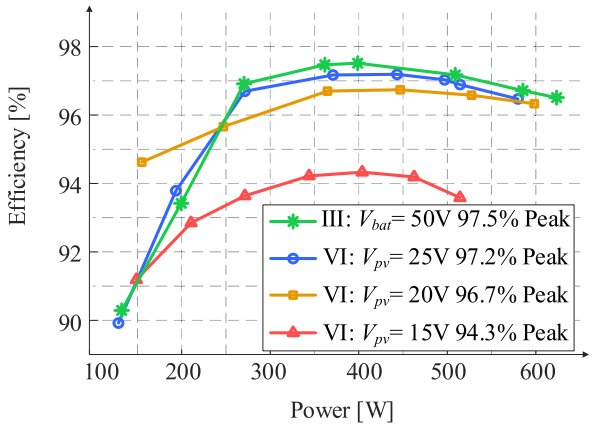

FIGURE 23. Measured efficiency versus output power with different PV voltages.

v_{ds} is zero. Those soft-switching conditions ensure efficient operation by reducing switching losses.

Fig. 22 illustrates the dynamic waveforms during power and operation mode transitions. Fig. 22(a) shows the power transition resulting from a step change in the PV source. In this case, the energy router operates in Mode VI, where both the PV source and the battery provide power to the dc bus. As seen in this figure, the power from the PV source jumps from 10 W to 200 W instantaneously, while the dc bus power remains constant at 500 W. Consequently, the currents i_{L_1}, i_{L_2}, and i_{pv} experience a sudden increase. To maintain the dc bus power, the battery side power is reduced, and the total power flow through the energy router remains constant during the transition. As observed, there is minimal effect on i_p and i_{L_k} during this process. Fig. 22(b) demonstrates the dynamic waveforms during the operation mode transition from Mode VI to Mode III, emulating the transition from daytime to nighttime operation. During this transition, the battery compensates for the decrease in PV power to maintain the dc bus power, P_{dc}, which is set to 400 W in this experiment. The transition occurs smoothly without any noticeable transients, which confirms the excellent dynamic performance of the proposed energy router.

Conversion efficiency at different modes and input voltages is recorded and plotted in Fig. 23. The efficiency data is calibrated using a high-precision power analyzer (LMG641 from ZIMMER Ltd). In Mode III, the efficiency is measured under the conditions $V_{bat} = 50$ V and $V_{dc} = 800$ V, with a peak efficiency of 97.5%. In Modes IV-VI, the efficiency is

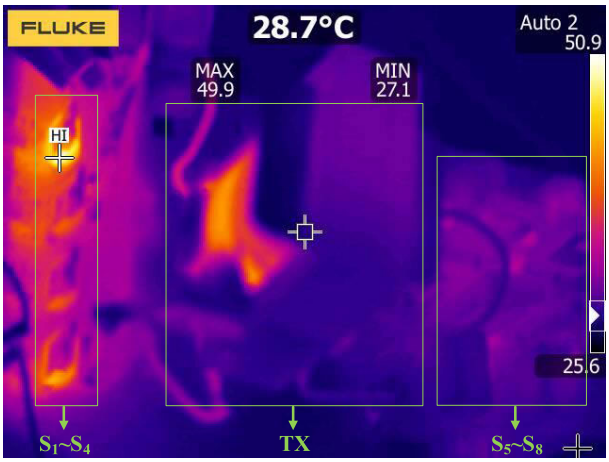

FIGURE 24. Temperature distribution of the prototype after operating at 550*W* for 30 minutes.

measured for $V_{pv} = 15$ V, 25 V, and 25 V, respectively. Only the efficiency data for Mode VI, where all ports are actively involved in power flow, is presented. The peak efficiency for the different input voltages of $V_{pv} = 25$ V, 20 V, and 15 V are 97.2%, 96.7%, and 94.3%, respectively. The overall efficiency remains above 90% across the entire power range in all operation modes. Compared to the efficiency at heavy load, the light-load efficiency decreases when the power is below 200 W due to the loss of ZVS in light-load conditions. Additionally, the efficiency curve for $V_{pv} = 25$ V drops faster than those for $V_{pv} = 15$ V and 20 V. This is because the duty cycle for $V_{pv} = 25$ V is 50%, resulting in a two-level voltage (v_{ab}) on the LV side, whereas the other two cases exhibit a three-level voltage on the LV side.

A thermal image (Fig.24) showing the temperature distribution of the prototype after operating at 550W for 30 minutes.The highest temperature observed was below 50°C, demonstrating acceptable thermal stability under the condition of exceeding the rated load, and the reliability of the design margin is verified.

B. PERFORMANCE COMPARISON

A qualitative comparison between the proposed energy router and several recently reported partially isolated energy routers and high boost ratio converters is summarized in Table 4. As shown, the proposed solution offers flexible power flow control through a combination of PWM and PSM, while maintaining a simplified structure without the need for additional components. Notably, unlike conventional control methods that require complex modulations or inner phase shifts on both sides, the proposed topology only requires phase-shift modulation between the LV and HV sides, without the need for internal phase shifts or PFM modulation. Additionally, without increasing the number of switches and inductors, the proposed energy router is characterized by a medium ZVS range, multidirectional power flow, and high efficiency. In addition, compared to high boost ratio converters, the proposed energy router achieves a higher

TABLE 4. Comparison with existing reported partially isolated energy routers and high boost ratio converters.

Converters	Ref.	Modulation	V_{in}[V]		V_{dc} [V]	No. of components			ZVS*	Bi-dir§	$\eta(\%)^{\dagger}$	Voltage ratio
			V_{pv}[V]	V_{bat}[V]		*S.*	*L*	*C*				
Energy routers	[13]	PWM+PFM+PSM	200	60-110	65	8	4	4	W	No	92	0.32
	[15]	PWM+PSM	70-100	42	300	8	3	4	W	No	97.6	7.1
	[16]	PWM	45	90	380	6	2	6	W	No	95.6	8.4
	[20]	PWM+PFM+PSM	70-100	180-210	400	8	3	3	W	Yes	98	5.7
	[33]	PWM+PSM	20-40	60	760	10	3	8	W	No	98.2	38
This work	-	**PWM+PSM**	15-40	40-50	800	**8**	**2**	**6**	M	**Yes**	**97.5**	**53**
High boost ratio converters	[14]	PWM	35-45		380	6	3	3	M	Yes	97.3	11
	[23]	PWM+PSM	20		400	8	2	7	N	No	96	20
	[27]	PWM	38-48		380	10	3	5	W	No	96.4	10
	[28]	PWM	30-60		600	7	3	7	N	No	94	20
	[29]	PWM	42		400	6	2	6	M	No	97.1	10
	[31]	PWM+PSM	20-28		380	8	3	5	W	No	96.3	19
	[32]	PWM	26		380	6	0	5	M	Yes	95.8	15

· S. stands for switches, including all passive switches and active switches
* ZVS range: W = Wide, M = Medium, N = Narrow.
§ 'Yes' indicates bidirectional power flow, while 'No' denotes unidirectional power flow.
† $\eta(\%)$ shows the peak efficiency within all the working modes.

boost ratio and offers the advantage of bidirectional power flow.

VII. CONCLUSION

This manuscript presents a novel energy router topology to achieve high step-up ratio, multidirectional power flow, and efficiency across a wide input voltage range simultaneously in 800V dc microgrid applications. By incorporating a VQC with an interleaved boost stage and a full-bridge stage, the energy router achieves high boost ratio, reduced component count, and balanced voltage stress on both capacitors and MOSFETs. A hybrid modulation scheme combining PWM and PSM is introduced. The hybrid modulation scheme ensures ZVS and minimizes circulating current, optimizing efficiency and enhancing system reliability. Experimental results demonstrate efficient operation with input voltages ranging from 15 V to 25 V at the PV port, delivering a high output voltage of 800 V and a rated power of 500 W. The peak efficiency reaches 97.5%, with the overall efficiency exceeding 90% in various operating modes and power levels, demonstrating excellent dynamic response and minimal voltage stress. Comparative analysis also highlights the superior performance of the proposed energy router in modulation simplicity, efficiency, and operational flexibility.

REFERENCES

[1] Int. Energy Agency. (2025). *Electricity 2025—Analysis*. [Online]. Available: https://www.iea.org/reports/electricity-2025

[2] A. K. Bhattacharjee, N. Kutkut, and I. Batarseh, "Review of multiport converters for solar and energy storage integration," *IEEE Trans. Power Electron.*, vol. 34, no. 2, pp. 1431–1445, Feb. 2019. [Online]. Available: https://ieeexplore.ieee.org/document/8352059

[3] P. Roy, J. He, T. Zhao, and Y. V. Singh, "Recent advances of wind-solar hybrid renewable energy systems for power generation: A review," *IEEE Open J. Ind. Electron. Soc.*, vol. 3, pp. 81–104, 2022. [Online]. Available: https://ieeexplore.ieee.org/document9684974/?arnumber=9684974

[4] G. Wang, H. Wen, P. Xu, W. Liu, J. Zhou, and Y. Yang, "A comprehensive review of integrated three-port DC–DC converters with key performance indices," *IEEE Trans. Power Electron.*, vol. 39, no. 5, pp. 6391–6408, Feb. 2024. [Online]. Available: https://ieeexplore.ieee.org/document/10439655

[5] Z. Wang, Q. Luo, Y. Wei, D. Mou, X. Lu, and P. Sun, "Topology analysis and review of three-port DC–DC converters," *IEEE Trans. Power Electron.*, vol. 35, no. 11, pp. 11783–11800, Nov. 2020. [Online]. Available: https://ieeexplore.ieee.org/document/9057408

[6] P. Luo, T.-J. Liang, K.-H. Chen, S.-M. Chen, and J.-F. Chen, "Syntheses of three-port DC–DC converters," *IEEE Trans. Power Electron.*, vol. 38, no. 12, pp. 16196–16207, Dec. 2023. [Online]. Available: https://ieeexplore.ieee.org/document/10238829/?arnumber=10238829

[7] S. Jalilyan, V. Abbasi, S. Ahmadian, A. R. Varmenjeh, and F. Y. Moghadam, "High step-up three-port DC–DC converter with few limitations in performance suitable for stand-alone renewable energy applications," *IEEE Trans. Ind. Electron.*, vol. 71, no. 10, pp. 12389–12401, Oct. 2024. [Online]. Available: https://ieeexplore.ieee.org/document/10438061

[8] Z. Lin, S. Pan, M. Wang, W. Lin, J. Gong, L. Yao, and P. Jain, "A three-port LCC resonant converter for the 380-V/48-V hybrid DC system," *IEEE Trans. Power Electron.*, vol. 37, no. 9, pp. 10864–10876, Sep. 2022. [Online]. Available: https://ieeexplore.ieee.org/document/9756851

[9] F. Hoffmann, J. Person, M. Andresen, M. Liserre, F. D. Freijedo, and T. Wijekoon, "A multiport partial power processing converter with energy storage integration for EV stationary charging," *IEEE J. Emerg. Sel. Topics Power Electron.*, vol. 10, no. 6, pp. 7950–7962, Dec. 2022. [Online]. Available: https://ieeexplore.ieee.org/document/9504546

[10] N. D. Dao, D.-C. Lee, and Q. D. Phan, "High-efficiency SiC-based isolated three-port DC/DC converters for hybrid charging stations," *IEEE Trans. Power Electron.*, vol. 35, no. 10, pp. 10455–10465, Oct. 2020. [Online]. Available: https://ieeexplore.ieee.org/document/9005173

[11] P. Gunawardena, N. Hou, D. Nayanasiri, and Y. Li, "A dual-input single-output DC–DC converter topology for renewable energy applications," *IEEE Trans. Ind. Appl.*, vol. 59, no. 2, pp. 1995–2006, Mar. 2023. [Online]. Available: https://ieeexplore.ieee.org/document/9933832

[12] R.-J. Wai, C.-Y. Lin, and Y.-R. Chang, "High step-up bidirectional isolated converter with two input power sources," *IEEE Trans. Ind. Electron.*, vol. 56, no. 7, pp. 2629–2643, Jul. 2009. [Online]. Available: https://ieeexplore.ieee.org/document/4812088

[13] X. Li, N. Li, W. Xue, W. Mao, S. Qiu, and X. Wu, "*LCC*-resonant-type current-fed-out three-port DC–DC converter for PV electrolytic hydrogen production integrated with energy storage," *IEEE Trans. Ind. Electron.*, vol. 72, no. 5, pp. 4910–4921, Oct. 2024. [Online]. Available: https://ieeexplore.ieee.vorg/document/10739865/?arnumber=10739865&tag=1

[14] H. Seok, B. Han, B.-H. Kwon, and M. Kim, "High step-up resonant DC–DC converter with ripple-free input current for renewable energy systems," *IEEE Trans. Ind. Electron.*, vol. 65, no. 11, pp. 8543–8552, Nov. 2018. [Online]. Available: https://ieeexplore.ieee.org/document/8322291

[15] H. Wu, J. Zhang, X. Qin, T. Mu, and Y. Xing, "Secondary-Side-Regulated soft-switching full-bridge three-port converter based on bridgeless boost rectifier and bidirectional converter for multiple energy interface," *IEEE Trans. Power Electron.*, vol. 31, no. 7, pp. 4847–4860, Jul. 2016. [Online]. Available: https://ieeexplore.ieee.org/document/7222483

[16] M. Zhou, C. Liu, R. Xie, Y. Zhuang, X. Mao, and Y. Zhang, "A high-gain three-port DC–DC converter with soft-switching for renewable energy system applications," *IEEE Trans. Power Electron.*, vol. 40, no. 1, pp. 1508–1518, Oct. 2024. [Online]. Available: https://ieeexplore.ieee.org/document/10723771/?arnumber=10723771

[17] X. Sun, Y. Shen, W. Li, and H. Wu, "A PWM and PFM hybrid modulated three-port converter for a standalone PV/battery power system," *IEEE J. Emerg. Sel. Topics Power Electron.*, vol. 3, no. 4, pp. 984–1000, Dec. 2015. [Online]. Available: https://ieeexplore.ieee.org/document/7089166

[18] X. Sun, Y. Shen, Y. Zhu, and X. Guo, "Interleaved boost-integrated LLC resonant converter with fixed-frequency PWM control for renewable energy generation applications," *IEEE Trans. Power Electron.*, vol. 30, no. 8, pp. 4312–4326, Aug. 2015. [Online]. Available: https://ieeexplore.ieee.org/document/6899684

[19] H. Wu, P. Xu, H. Hu, Z. Zhou, and Y. Xing, "Multiport converters based on integration of full-bridge and bidirectional DC–DC topologies for renewable generation systems," *IEEE Trans. Ind. Electron.*, vol. 61, no. 2, pp. 856–869, Feb. 2014. [Online]. Available: https://ieeexplore.ieee.org/document/6484965

[20] L. Wang, H. Wang, M. Fu, J. Liang, and Y. Liu, "A three-port energy router for grid-tied PV generation systems with optimized control methods," *IEEE Trans. Power Electron.*, vol. 38, no. 1, pp. 1218–1231, Jan. 2023. [Online]. Available: https://ieeexplore.ieee.org/document/9870571

[21] J. Zhang, H. Wu, X. Qin, and Y. Xing, "PWM plus secondary-side phase-shift controlled soft-switching full-bridge three-port converter for renewable power systems," *IEEE Trans. Ind. Electron.*, vol. 62, no. 11, pp. 7061–7072, Nov. 2015. [Online]. Available: https://ieeexplore.ieee.org/document/7131521

[22] V. A. K. Prabhala, P. Fajri, V. S. P. Gouribhatla, B. P. Baddipadiga, and M. Ferdowsi, "A DC–DC converter with high voltage gain and two input boost stages," *IEEE Trans. Power Electron.*, vol. 31, no. 6, pp. 4206–4215, Jun. 2016. [Online]. Available: https://ieeexplore.ieee.org/document/7239618

[23] A. Alzahrani, M. Ferdowsi, and P. Shamsi, "High-voltage-gain DC–DC step-up converter with bifold Dickson voltage multiplier cells," *IEEE Trans. Power Electron.*, vol. 34, no. 10, pp. 9732–9742, Oct. 2019. [Online]. Available: https://ieeexplore.ieee.org/document/8598986

[24] S. Park, J. Yang, and J. Rivas-Davila, "A hybrid cockcroft–Walton/Dickson multiplier for high voltage generation," *IEEE Trans. Power Electron.*, vol. 35, no. 3, pp. 2714–2723, Mar. 2020. [Online]. Available: https://ieeexplore.ieee.org/document/8767979

[25] Q. Wu, W. Zhao, Q. Wang, and L. Xiao, "Low-ripple low-voltage-drop full-wave voltage multipliers for high voltage generation," *IEEE Trans. Power Electron.*, vol. 39, no. 11, pp. 14803–14814, Jul. 2024. [Online]. Available: https://ieeexplore.ieee.org/document/10609557/?arnumber=10609557

[26] Y. Zuo, X. Shen, and W. Martinez, "Reconfigurable LLC resonant converter for wide voltage range and reduced voltage stress in DC-connected EV charging stations," *IEEE Trans. Power Electron.*, vol. 40, no. 3, pp. 3838–3843, Mar. 2025. [Online]. Available: https://ieeexplore.ieee.org/document/10757368/?arnumber=10757368

[27] J. Yea and B. Han, "An isolated high-voltage-gain resonant converter utilizing voltage quadrupler with bi-directional-switch for fuel-cell applications," *IEEE Trans. Ind. Electron.*, vol. 72, no. 1, pp. 580–588, Jan. 2025. [Online]. Available: https://ieeexplore.ieee.org/document/10586746

[28] A. Nafari and R. Beiranvand, "An extendable interleaved quasi Z-source high step-up DC–DC converter," *IEEE Trans. Power Electron.*, vol. 38, no. 4, pp. 5065–5076, Apr. 2023. [Online]. Available: https://ieeexplore.ieee.org/document/10014547

[29] K. Kanathipan and J. Lam, "A high voltage gain isolated PV micro-converter with a single-voltage maximum power point tracking control loop for DC micro-grid systems," *IEEE J. Emerg. Sel. Topics Ind. Electron.*, vol. 3, no. 3, pp. 755–765, Jul. 2022. [Online]. Available: https://ieeexplore.ieee.org/document/9626562

[30] Y. Zhao, X. Xiang, W. Li, X. He, and C. Xia, "Advanced symmetrical voltage quadrupler rectifiers for high step-up and high output-voltage converters," *IEEE Trans. Power Electron.*, vol. 28, no. 4, pp. 1622–1631, Apr. 2013. [Online]. Available: https://ieeexplore.ieee.org/document/6257500

[31] Y. Lu, Y. Xing, and H. Wu, "A PWM plus phase-shift controlled interleaved isolated boost converter based on semiactive quadrupler rectifier for high step-up applications," *IEEE Trans. Ind. Electron.*, vol. 63, no. 7, pp. 4211–4221, Jul. 2016. [Online]. Available: https://ieeexplore.ieee.org/document/7437429

[32] K. R. Kothapalli, M. R. Ramteke, and H. M. Suryawanshi, "ZVS–ZCS high step-up/step-down isolated bidirectional DC–DC converter for DC microgrid," *IEEE Trans. Power Electron.*, vol. 38, no. 6, pp. 7733–7745, Jun. 2023. [Online]. Available: https://ieeexplore.ieee.org/abstract/document/9896869

[33] J. Deng, H. Wang, and M. Shang, "A ZVS three-port DC/DC converter for high-voltage bus-based photovoltaic systems," *IEEE Trans. Power Electron.*, vol. 34, no. 11, pp. 10688–10699, Nov. 2019. [Online]. Available: https://ieeexplore.ieee.org/document/8629308

[34] M. Forouzesh, Y. P. Siwakoti, S. A. Gorji, F. Blaabjerg, and B. Lehman, "Step-up DC–DC converters: A comprehensive review of voltage-boosting techniques, topologies, and applications," *IEEE Trans. Power Electron.*, vol. 32, no. 12, pp. 9143–9178, Dec. 2017. [Online]. Available: https://ieeexplore.ieee.org/document/7872494

[35] Y. Peng, B. Xue, L. Wang, and H. Wang, "An active voltage quadrupler rectifier based multidirectional three-port converter in 800 V microgrids," in *Proc. IEEE Appl. Power Electron. Conf. Expo. (APEC)*, Feb. 2024, pp. 1255–1260. [Online]. Available: https://ieeexplore.ieee.org/abstract/document/10509176

[36] P. C. Sahu, "Impact and integration of electric vehicles on renewable energy based microgrid: Frequency profile improvement by a-SCA optimized FO-fuzzy PSS approach," *Green Energy Intell. Transp.*, vol. 4, no. 2, Apr. 2025, Art. no. 100191. [Online]. Available: https://www.sciencedirect.com/science/article/pii/S2773153724000434

[37] K. B. Samal, S. Pati, and R. Sharma, "Power management using an improved EMS algorithm in a stand-alone hybrid PV-PEMFC microgrid with reduced converter count," *Green Energy Intell. Transp.*, Apr. 2025, Art. no. 100302. [Online]. Available: https://www.sciencedirect.com/science/article/pii/S2773153725000520

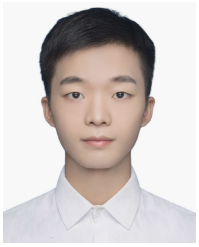

YUCHONG PENG (Student Member, IEEE) received the B.S. degree in rail transit signal and control from the Central South University, Changsha, China, in 2022. He is currently pursuing the M.S. degree with the School of Information Science and Technology, ShanghaiTech University, Shanghai, China. His research interests include energy router, three-port converters, and dual active bridge converter.

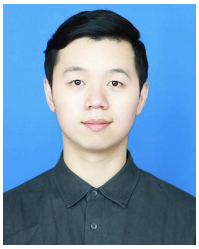

JIAWEI LIANG (Student Member, IEEE) received the bachelor's degree in electronic information engineering from ShanghaiTech University, Shanghai, China, in 2020, where he is currently pursuing the Ph.D. degree in electrical engineering with the School of Information Science and Technology. His current research interests include voltage regulator modules and magnetic integration in data center applications.

HAOYU WANG (Senior Member, IEEE) received the bachelor's degree (Hons.) in electrical engineering from Zhejiang University, Hangzhou, China, in 2009, and the Ph.D. degree in electrical engineering from the University of Maryland, College Park, MD, USA, in 2014.

In September 2014, he joined the School of Information Science and Technology, where he is currently a Full Professor with Tenure. His research interests include power electronics, electric vehicles, the applications of wide-bandgap semiconductors, renewable energy systems, and power management integrated circuits.

Dr. Wang is an Associate Editor of IEEE TRANSACTIONS ON INDUSTRIAL ELECTRONICS, IEEE TRANSACTIONS ON TRANSPORTATION ELECTRIFICATION, and *CPSS Transactions on Power Electronics and Applications*. He is also a Guest Editor of IEEE JOURNAL OF EMERGING AND SELECTED TOPICS IN POWER ELECTRONICS and IEEE TRANSACTIONS ON POWER ELECTRONICS.